

High-Temperature Oxidation of FeCr(Ni) Alloys: The Behaviour After Breakaway

T. Jonsson¹ · H. Larsson² · S. Karlsson¹ ·
H. Hooshyar¹ · M. Sattari¹ · J. Liske¹ · J.-E. Svensson¹ ·
L.-G. Johansson¹

Received: 21 December 2016 / Published online: 7 February 2017

© The Author(s) 2017. This article is published with open access at Springerlink.com

Abstract The oxidation of an austenitic FeCr(Ni) steel at 600 °C in H₂O + KCl + O₂/H₂ + H₂O + Ar environments is studied up to 168 h. The oxidation behaviour after “breakaway” is investigated by microstructural investigations, and thermodynamic calculations (Thermo-Calc) on the FeCr(Ni)–O system are used to interpret the results. The characteristic “breakaway” scale morphology exhibits an outward-growing iron oxide and a bottom layer consisting of inward-growing spinel oxide and reaction zones containing Cr-rich oxide precipitates and Cr-depleted metal. The equilibrium calculations show that a miscibility gap appears in the FeCr spinel oxide below 665 °C influencing the microstructure of the inward-growing scale. Equilibrium calculations on the FeCrNi–O system show that Ni is not expected to enter the spinel oxide in low oxygen activity conditions, in accordance with observations.

Keywords High-temperature oxidation · Breakaway corrosion · Stainless steel · Internal oxidation

Introduction

High-temperature stainless steels are designed to form a dense, slow-growing Cr-rich oxide scale at high temperatures. However, in demanding applications the materials can suffer a sudden acceleration of oxidation, referred to as “breakaway oxidation”, which is accompanied by a change in the composition and microstructure of the scale. The mechanisms of breakdown of the initial highly protective Cr-

✉ T. Jonsson
tj@chalmers.se

¹ Environmental Inorganic Chemistry, Department of Chemistry and Chemical Engineering, Chalmers University of Technology, 412 96 Göteborg, Sweden

² Thermo-Calc Software, Råsundavägen 18, SE-169 67 Solna, Sweden

rich oxide scale have been studied in various environments, see, e.g. Refs. [1–5]. The useful life of an alloy component that suffers breakaway oxidation depends both on the incubation time prior to breakaway and on the scale growth rate after breakaway. Generally, the scales observed on stainless steels after breakaway consist of an outward-growing iron-rich oxide layer and a complex inward-growing layer, see, e.g. Refs. [1–5]. A recent paper describes the detailed microstructure of several cases of “breakaway scales” observed on a FeCrNi stainless steel that had been exposed to a variety of environments at 600 °C [6]. The microstructure of the inward-growing part of the scale was essentially the same irrespective of environment/alloy and exposure environment. It consisted of alternating, fully oxidized regions, made up of spinel oxide, and partially oxidized alloy. The latter consisted of a mixture of Cr-depleted metal and FeCr spinel oxide. The aim of the present paper is to investigate generic properties of the scales formed on stainless steel (304L) after breakdown of the initial protective scale. The work involves a detailed microstructural investigation of the oxide scales formed after breakaway (up to 168 h) in different corrosive environments and thermodynamic equilibrium calculations on the FeCr–O and FeCrNi–O systems.

Experimental Procedures

The investigated materials in this study are two grades of 304L stainless steel with the nominal compositions given in Table 1. Samples with the dimensions of $15 \times 15 \times 2$ mm were cut and ground down to P1000 SiC paper followed by polishing with diamond suspension down to 1 μm particle size and then rinsed in water/cleaned in acetone and ethanol ultrasonic bath.

Oxidation experiments were carried out at 600 °C in a tube furnace with the gas flow parallel to the sample surface. The gas composition for the $\text{H}_2 + \text{H}_2\text{O}$ environment was as follows: 10% H_2 –20% H_2O –Ar giving an oxygen partial pressure of about 10^{-24} bar. The samples (18Cr–8Ni) were exposed for 72 h. The samples (18Cr–10Ni) exposed at a high PO_2 environment (5% $\text{O}_2 + 40\%\text{H}_2\text{O} + 55\%\text{N}_2$) were coated with KCl and exposed for 168 h. The salt was applied by spraying the samples with a saturated solution of the desired salt in water, water/ethanol or acetone. The amount of salt corresponded to a potassium content of $1.35 \mu\text{mol K}^+/\text{cm}^2$ ($0.10 \text{ mg}/\text{cm}^2$ in the case of KCl). More details about oxidation experiments can be found in Ref. [6]. Both environments caused breakaway oxidation, and a mass gain of $1.05 \text{ mg}/\text{cm}^2$ was recorded for the $\text{H}_2 + \text{H}_2\text{O}$ sample, while the KCl-coated sample recorded mass gain of $0.85 \text{ mg}/\text{cm}^2$. The oxide scales

Table 1 Nominal composition of the studied 304L stainless steels (wt%)

Element	Fe	Cr	Ni	Mn	Si
18Cr10Ni	Bal.	18.5	10.2	1.41	0.55
18Cr8Ni	Bal.	18.8	8.10	1.53	0.31

were characterized using scanning electron microscopy (SEM) imaging and analytical scanning transmission electron microscopy (STEM). For the purpose of STEM analysis a site-specific thin cross section of the sample was prepared by focus ion beam (FIB) milling and in situ lift-out technique in an FEI Versa™ 3D DualBeam™ instrument. Prior to milling a layer of Pt was deposited on the region of interest in order to provide protection against ion beam damage. Analytical scanning transmission electron microscopy (STEM) investigations of the oxide scale were carried out using an FEI Titan 80–300 microscope operating at an accelerating voltage of 300 kV. Chemical analysis of the oxide scale was done by energy-dispersive X-ray spectroscopy (EDS) using an INCA X-Sight Oxford Instrument detector coupled to the microscope. All data acquisition and post-processing were carried out in FEI TEM Imaging and Analysis (TIA) software. Thermodynamic calculations were performed using the Thermo-Calc program [7, 8] with the database TCFE7. CALPHAD databases are generally assessed for use with specific alloy systems. The TCFE7 thermodynamic database is tailored to Fe-base systems.

Results and Discussion

It is well known that FeCr and FeCrNi stainless steels exposed in mildly corrosive environments up to 600–700 °C form a thin protective external oxide [9–12]. The protectiveness of this scale is attributed to an inner layer consisting of $(\text{Cr}_x\text{Fe}_{1-x})_2\text{O}_3$ containing about 70% Cr (cationic). As noted in the introduction, this scale tends

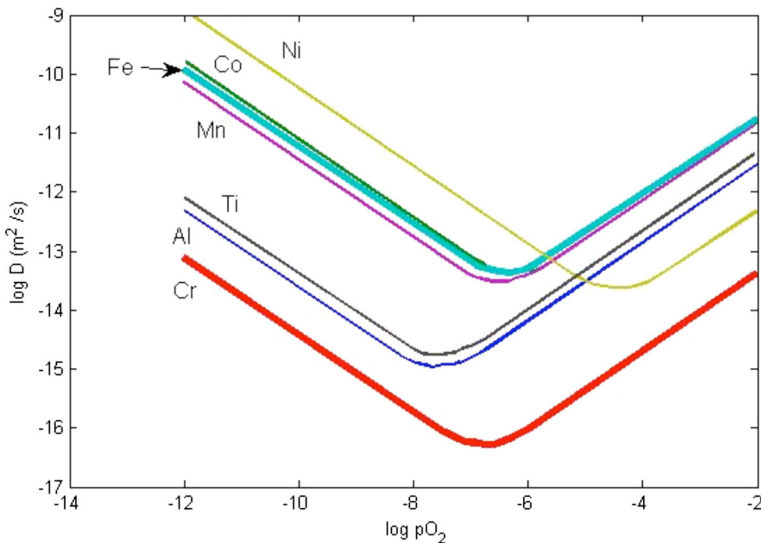


Fig. 1 Cation diffusion coefficients in magnetite at 1200 °C. Fe, Co, Cr, Al, and Ni were reported by Dieckmann and Schmalzried [23]. Mn and Ti were reported by Aggarwal and Dieckmann [24]. The data were summarized by Van Orman and Crispin [18]

to lose its protective properties under more corrosive conditions, e.g. when water vapour, traces of alkali and/or chlorides are combined with O_2 , and in low oxygen activity environments containing water vapour, see, e.g. Refs. [13–15]. The corresponding “breakaway” event is accompanied by a great acceleration of oxidation and in the appearance of a characteristic scale microstructure. This work focuses on the microstructure of oxidation observed *after* breakaway. The microstructure is interpreted using predictions provided by thermodynamic equilibrium calculations in the FeCr(Ni)–O system.

FeCr–O System

The oxide scales formed on stainless steels, in the temperature range 500–900 °C, directly after the breakaway event, have been characterized in several papers [5, 13–17]. The “breakaway scale” typically consists of an inward-growing part consisting of spinel oxide + internally oxidized alloy regions (reaction zones) and an outward-growing iron-rich oxide layer. The ratio inward/outward growth rate is given by the ratio of the anion/cation diffusivities. The two layers are separated by remnants of the initial protective scale, corresponding to the original metal/oxide interface, see, e.g. [1, 17]. This characteristic morphology may be interpreted in terms of the different diffusivities of Cr^{3+} and Fe^{2+} in the spinel phase. Figure 1

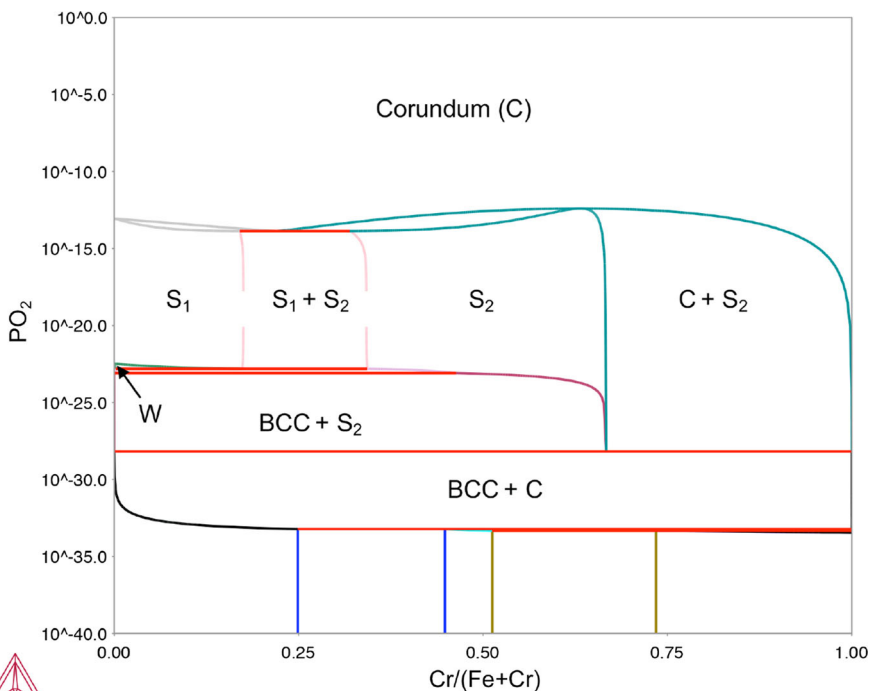


Fig. 2 Stable phases in the FeCr–O system at 650 °C as a function of oxygen activity and mole fraction of Cr calculated using the Thermo-Calc program with the database TCFE7. C = corundum-type M_2O_3 , $S_1 = Fe_{3-x}Cr_xO_4$, $S_2 = FeCr_{2-x}Fe_xO_4$, W = $Fe_{1-x}O$, BCC = ferrite-structured metal

shows the plot of the diffusivities of several cations in magnetite against oxygen activity at 1200 °C, (adapted after Van Orman and Crispin [18]). Roughly, the cations fall into two groups. The first group is made up of Fe, Co, Ni, Mn and exhibits orders of magnitude faster diffusivities than the second group of cations which includes Ti, Al and Cr. It may be noted that the first group of cations is often present in the divalent state in II/III spinel oxides while the second group ions are trivalent. In Wagner-type oxidation of metals, anions and cations migrate towards the scale/metal and scale/gas interfaces, respectively. If the data in Fig. 1 are taken to be representative of cation diffusivities of iron-containing spinels in the temperature range of interest, cations belonging to the first category (Fe^{2+} , Ni^{2+} , Mn^{2+}) are expected to diffuse relatively rapidly towards the gas/scale interface during oxidation while the cations belonging to the latter group (i.e. Cr^{3+}) are expected to move comparatively little from the spot where they originally formed. The width of the inward-growing oxide is expected to depend on the diffusivity of oxygen in the particular system. According to the assessment by Naraghi (unpublished research), the oxygen diffusivity in the magnetite is roughly two orders of magnitude lower than the diffusivity of iron. The assessment of the oxygen diffusivity is based on the experimental work in Refs. [19–22].

The characteristic microstructure following breakaway can be further elucidated by considering the FeCr–O system. When using equilibrium phase diagrams for interpreting corrosion morphologies, it must be kept in mind that corrosion is essentially a non-equilibrium process and that there is every reason to expect non-equilibrium (metastable) phases to appear in a corroded specimen. Also, phase

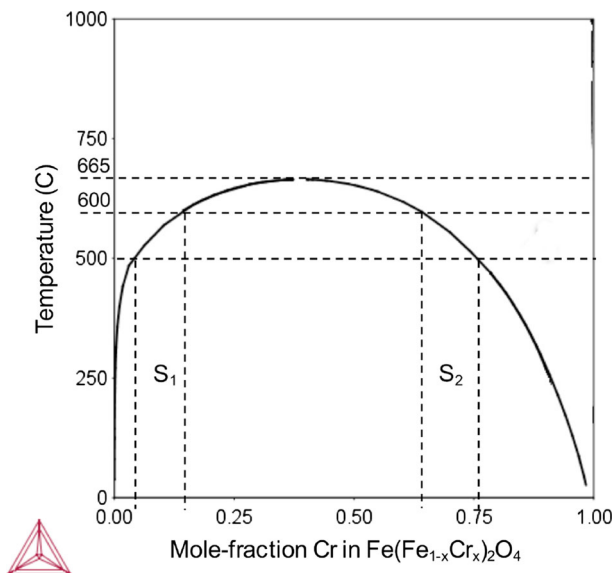


Fig. 3 Spinel miscibility gap as a function of temperature, calculated using the Thermo-Calc program and the database TCFE7. Mole-fraction on the axis represents mole fraction of Cr (cations) in the spinel phase; $X = 0$ represents Fe_3O_4 , while $X = 1$ represents FeCr_2O_4 . The miscibility gap closes at about 665 °C. The miscibility gap at 500 and 600 °C is illustrated by the *hatched lines*

diagrams, whether calculated or not, inherently have a degree of uncertainty. Nevertheless, there is reasonable agreement between the calculated FeCr–O phase diagrams and some of the experimental observations, see below.

Figure 2 shows equilibrium phases in the FeCr–O system at 650 °C as a function of oxygen activity and mole fraction of Cr, calculated using the Thermo-Calc program. Oxygen activity is highly relevant in oxidation as the driving force for diffusion in a Wagner-type scenario is the oxygen activity gradient across the scale. It may be noted that a miscibility gap appears in the $(\text{Fe,Cr})_3\text{O}_4$ spinel oxide phase corresponding to the region marked $S_1 + S_2$ in the figure.

Figure 3 shows the calculated temperature dependence of the spinel miscibility gap, showing that the gap diminishes with increasing temperature and disappears above about 665 °C. According to Fig. 3 the maximum solubility of Cr^{3+} at 500 and 600 °C in S_1 (=magnetite) is about 5 and 15%, respectively. On the S_2 (=FeCr₂O₄) side, the gap at 500 and 600 °C is at 75 and 65%, respectively, (100% representing FeCr₂O₄ in Fig. 3). The presence of a spinel miscibility gap may help explain some aspects of internal oxidation reported for FeCr and FeCrNi alloys, e.g. the composition of the internal oxide [1, 13, 14, 16, 17, 23]. This may be illustrated by the scale microstructure on a Fe–10Cr model alloy after breakaway oxidation where the reported composition of the oxide precipitates in the internally oxidized alloy (reaction zone) corresponded to the Cr-rich side of the miscibility gap [17].

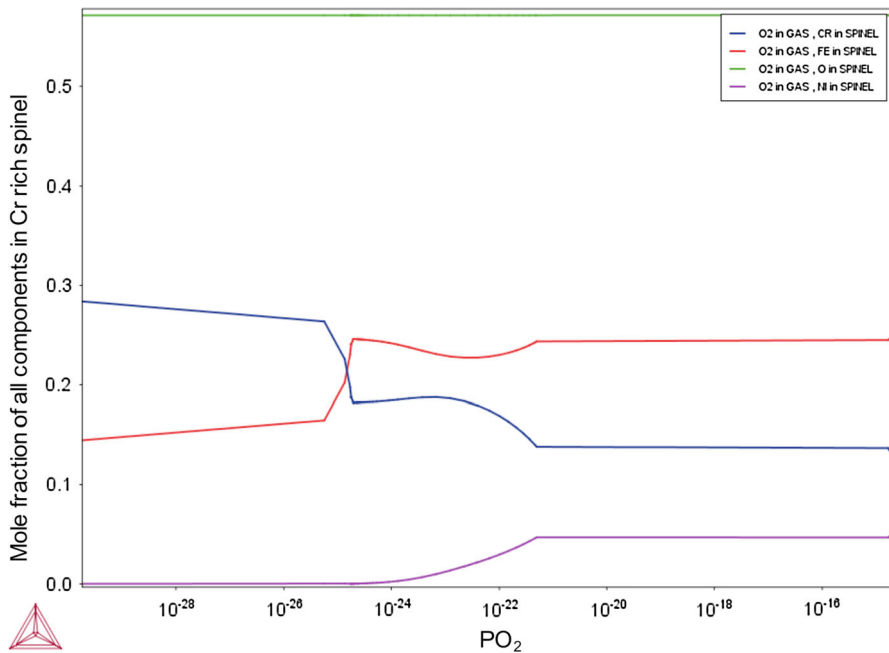


Fig. 4 Mole fraction of cations Fe, Cr and Ni in the Cr-rich spinel type structure (M_3O_4) versus oxygen activity at 600 °C calculated using the Thermo-Calc program with the database TCFE7. The metal composition corresponds to Fe18Cr10Ni alloy

FeCrNi–O System

Prior to breakaway oxidation, the Ni-containing stainless steels behave very similar to FeCr stainless steels, forming a protective Cr-rich corundum-type $(Cr_xFe_{1-x})_2O_3$ scale. Also, the development of scale microstructure after breakaway is similar to FeCr steels. Thus, the outward-growing scale typically consists of iron oxide, while the inward-growing spinel is enriched in Cr and Ni, see, e.g. Ref. [6]. In some cases, especially with alloys containing high levels of Ni, Ni^{2+} has been observed in the outward-growing scale, see, e.g. Ref. [24]. This is in accordance with Fig. 1 which predicts that Ni^{2+} will diffuse rapidly in the spinel, towards the scale/gas interface. Ni is often observed in the inward-growing part of the breakaway scale on FeCrNi stainless steels. Figure 4 shows the calculated equilibrium composition at 600 °C of

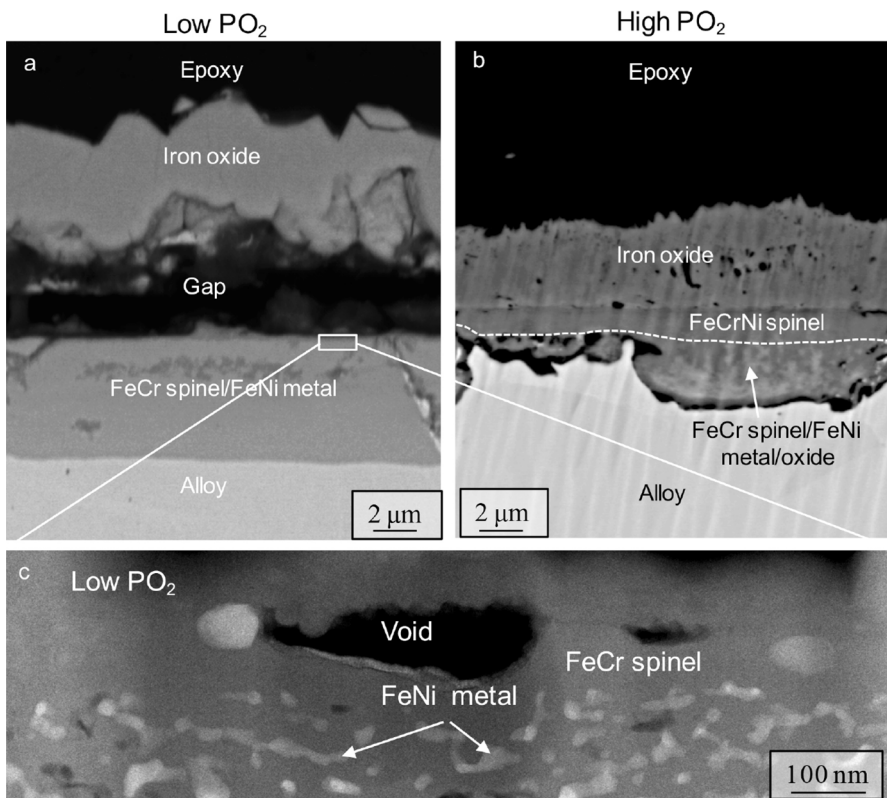


Fig. 5 **a** BSE image of a scale cross section of 304L stainless steel exposed 72 h in $10\%H_2 + 20\%H_2O + Ar$ at 600 °C (after breakaway); **b** BSE image of a scale cross section of 304L stainless steel exposed for 168 h in $5\%O_2 + 40\%H_2O + KCl$ at 600 °C (after breakaway). In both **a**, **b** the inward-growing part of the breakaway scale consists of darker, fully oxidized regions and brighter areas consisting of partially oxidized alloy (=reaction zones). In **a** the fully oxidized region is very thin and consists of iron chromium spinel. In **b** the fully oxidized layer is much thicker and consists of FeCrNi spinel oxide. **c** HAADF image corresponding to the boxed area in **(a)**, illustrating both the thin, fully oxidized region and the reaction zone. The latter consists of a mixture of Cr-depleted metal and 20–50 nm size Cr-rich spinel oxide precipitates. The precipitates correspond to the solid solution S_2 in Fig. 2

the Cr-rich spinel oxide (corresponding to the solid solution S_2 in Fig. 2), formed on an alloy with the composition Fe18Cr10Ni, as a function of oxygen activity. It may be noted that the oxygen activity dependence of the Ni^{2+} content is similar for the Cr-poor spinel (S_1 in Fig. 2). Figure 4 shows that the formation of Ni-containing spinel is spontaneous at oxygen activities $>10^{-24}$. At oxygen activities $<10^{-25}$, decomposition of the FeCr spinel oxide solid solution ($=S_2$) to $FeCr_2O_4$ + metallic iron becomes spontaneous.

The calculated phase diagram in Fig. 4 may be used to interpret the “breakaway” scale microstructures of 304L stainless steel exposed in two different corrosive environments, one being a high PO_2 environment and the other a H_2/H_2O environment with an oxygen activity of about 10^{-24} , see experimental section. Figure 5 shows BSE images of scale cross sections for the two cases. In both cases the expected scale microstructure was observed, with outward-growing iron oxide and inward-growing spinel oxide/internally oxidized alloy. However, the sample exposed at low oxygen activity showed a similar microstructure throughout the inward-growing scale, while the inward-growing scale developed at high PO_2 consisted of two layers (compare Fig. 5a, b). Thus, in the high PO_2 environment, the top, fully oxidized, part of the inward-growing scale contained Ni while internal oxidation was observed in the lower part, for details see Ref. [6]. This indicates that the oxygen activity at the interface between the internally oxidized metal and the fully oxidized layer has been $>10^{-24}$, allowing Ni to oxidize and enter into the spinel. In the low PO_2 environment, the inward-growing spinel does not contain Ni (based on TEM/EDX measurements), see HAADF image in Fig. 5c. This is in agreement with Fig. 4 which shows that the Ni-containing spinel is thermodynamically unstable at the oxygen activity of the gas phase (in this case about 10^{-24}).

Conclusions

- The scale formed on stainless steels after breakaway oxidation typically exhibits an inward-growing part consisting of Cr-rich spinel oxide + internally oxidized alloy and an outward-growing iron-rich oxide layer. The observed elemental distributions in the scale are partly explained by the different diffusivities of, e.g. Cr^{3+} and Fe^{2+} in spinel oxide. The ratio inward/outward growth rate is given by the ratio of the anion/cation diffusivities.
- Thermodynamic calculations indicate a miscibility gap in the $(FeCr)_3O_4$ spinel solid solution below about 665 °C
- Within the inward-growing scale, the internally oxidized alloy consisted of a mixture of 20–50 nm size Cr-rich spinel oxide precipitates and Cr-depleted alloy. After exposure at 600 °C, the composition of the oxide precipitates was on the high-chromium side of the miscibility gap.
- The microstructure of the “breakaway” scales on FeCrNi stainless steels was similar to that observed on FeCr stainless steels. Ni^{2+} entered the (fully oxidized) part of the inward-growing scale in high PO_2 environment but not in

H₂/H₂O environment. This behaviour is interpreted in terms of the influence of oxidation potential on the equilibrium composition of the spinel oxide.

Acknowledgements This work was carried out within the High Temperature Corrosion Centre (HTC) at Chalmers University of Technology and with support from VINNOVA, Sweden's Innovation Agency, within the Metallic Materials programme. The authors are grateful to Dr. Samuel Hallström and Dr. Lina Kjellqvist at Thermo-Calc software AB for discussing the Thermo-Calc calculations.

Open Access This article is distributed under the terms of the Creative Commons Attribution 4.0 International License (<http://creativecommons.org/licenses/by/4.0/>), which permits unrestricted use, distribution, and reproduction in any medium, provided you give appropriate credit to the original author(s) and the source, provide a link to the Creative Commons license, and indicate if changes were made.

References

1. B. Pujilaksono, et al., *Oxidation of Metals* **75**, (3), 2011 (183–207).
2. A. N. Hansson, et al., *Oxidation of Metals* **73**, (1–2), 2010 (289–309).
3. E. Essuman, et al., *Scripta Materialia* **57**, (9), 2007 (845–848).
4. D. J. Young, et al., *Corrosion Science* **53**, (6), 2011 (2131–2141).
5. G. H. Meier, et al., *Oxidation of Metals* **74**, (5–6), 2010 (319–340).
6. T. Jonsson, et al., *Oxidation of Metals*, 2016 (1–28).
7. J. O. Andersson, et al., *Calphad* **26**, 2002 (273–312).
8. B. Sundman, *Journal of Phase Equilibria* **12**, 1991 (127–140).
9. H. Asteman, et al., *Oxidation of Metals* **54**, 2000 (11–26).
10. B. Pujilaksono, et al., *Oxidation of Metals* **75**, (3–4), 2011 (183–207).
11. N. K. Othman, et al., *Corrosion Science* **51**, (12), 2009 (3039–3049).
12. N. K. Othman, J. Q. Zhang and D. J. Young, *Oxidation of Metals* **73**, (1–2), 2010 (337–352).
13. M. Halvarsson, et al., *Corrosion Science* **48**, (8), 2006 (2014–2035).
14. T. Jonsson, et al., *Oxidation of Metals* **72**, (3), 2009 (213–239).
15. Jonsson, T., et al., *Oxidation of Metals* **81**, (5–6), 2014 (575–596).
16. T. Jonsson, et al., *Journal of The Electrochemical Society* **154**, (11), 2007 (C603–C610).
17. T. Jonsson, et al., *Corrosion Science* **75**, 2013 (326–336).
18. J. A. Van Orman and K. L. Crispin, in *Diffusion in Minerals and Melts*, eds. Y. X. Zhang and D. J. Cherniak (Mineralogical Soc Amer, Chantilly, 2010), pp. 757–825.
19. J. E. Castle and P. L. Surman, *Journal of Physical Chemistry* **73**, (3), 1969 (632–634).
20. A. G. Crouch and J. Robertson, *Acta Metallurgica Et Materialia* **38**, (12), 1990 (2567–2572).
21. F. Millot and Y. Niu, *Journal of Physics and Chemistry of Solids* **58**, (1), 1997 (63–72).
22. F. Millot, et al., *Berichte Der Bunsen-Gesellschaft-Physical Chemistry Chemical Physics* **101**, (9), 1997 (1351–1354).
23. Dieckmann, R. and H. Schmalzried, *Berichte Der Bunsen-Gesellschaft-Physical Chemistry Chemical Physics* **90**, (7), 1986 (564–575).
24. Aggarwal, S. and R. Dieckmann, *Physics and Chemistry of Minerals* **29**, (10), 2002 (695–706).